# RSC Advances

This is an *Accepted Manuscript*, which has been through the Royal Society of Chemistry peer review process and has been accepted for publication.

Accepted Manuscripts are published online shortly after acceptance, before technical editing, formatting and proof reading. Using this free service, authors can make their results available to the community, in citable form, before we publish the edited article. This *Accepted Manuscript* will be replaced by the edited, formatted and paginated article as soon as this is available.

You can find more information about *Accepted Manuscripts* in the **Information for Authors**.
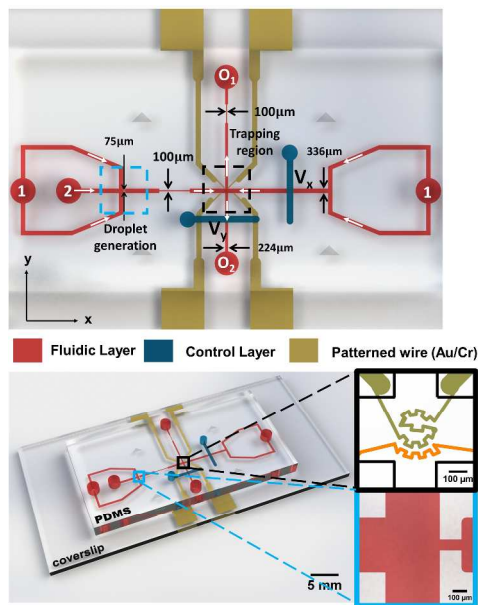
Nematic-to-isotropic transition of trapped single liquid crystal droplet under temperature ramp
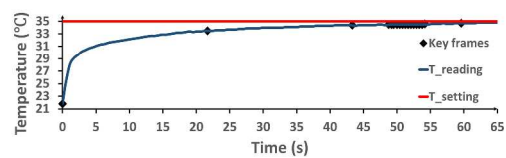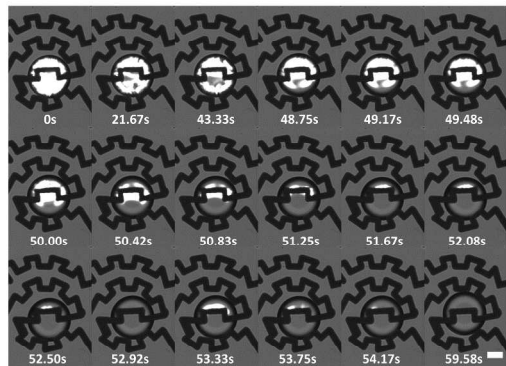
1690x1032mm (72 x 72 DPI)

Journal Name

Integrated microfluidic platform for instantaneous flow and localized temperature control[†]

Cifeng Fang,[‡a] Doojin Lee,[‡b] Boris Stober,[c] Gerald G. Fuller,[d] and Amy Q. Shen[*a,b]

We developed an integrated microfluidic platform for instantaneous flow and localized temperature control. The platform consisted of a flow-focusing region for emulsion droplet production, a cross-junction region embedded with a microheater for droplet trapping and localized temperature control by using an active feedback control system. The droplet trapping performance and trapping stability were also investigated. We further used thermotropic liquid crystal as the droplet phase to demonstrate the trapping and temperature control ability of the microfluidic platform. Our integrated platform offers the capability of manipulating non-contact, instantaneous flow with localized temperature control, which provides valuable tools for studying transient interfacial dynamics and various biological and industrial processes.

1 Introduction

Microfluidics is the science and technology of systems that manipulate small (picoliters to microliters) quantities of fluids, with the device characteristic length scales ranging from tens to hundreds of micrometers.[1] Microfluidics has emerged as a versatile method of handling fluids at small length-scales, with advantages in low reagent cost, high resolution and sensitivity, fast prototyping, short analysis time, and a well controlled microenvironment in concentration, pH, and temperature[2–7]. In particular, microfluidics has been employed to generate double emulsion droplets,[8] Janus particles,[9] enhanced mixing,[10] cell encapsulations,[11] focusing and sorting cells and particles,[12] and stretching DNA and deformable cells at cross-slot microchannels[13,14]. Among them, precise trapping and manipulation of suspended objects in fluids (e.g., particles, long chain molecules, drops and cells), is challenging but particularly useful for operations such as flow cytometry, cell-on-chip,[15–17] microfluidic crystallization,[7] and isolation of rare cells from solutions. Simultaneous control of flow and temperature on a single device is more difficult to achieve, yet critical for a wide range of applications such as polymerase chain reaction (PCR)[18,19] and chemical reactions.[18,20,21]

1.1 Flow control

Various passive methods to manipulate objects in microfluidics have been reported, such as inertial migration,[22] pinched flow fractionation (PFF),[23] deterministic lateral displacement,[24] and hydrodynamic chromatography.[25] These methods are limited to the high-throughput focusing and sorting, but lack of precise trapping of the objects at a specific zone. Alternatively, several active strategies have been explored for trapping and manipulating suspended objects in fluids, by applying external driving forces such as acoustic,[26,27] optical,[28] electrophoretic,[29] magnetic,[30] and hydrodynamic[31] techniques. Each active manipulation method has its own limitations. For example, the acoustic and magnetic methods are limited by their fabrication techniques to scale down the device; the electrophoretic method requires an ionic working fluid since it uses a charged interface between the particle surface and surrounding fluid; the optical method generates limited force range ($0.1 \sim 100$ pN), which is only suitable to manipulate nano or sub-micron scale objects. The hydrodynamic method offers several advantages for trapping and manipulating single objects with high spatial resolution on chip without the need for additional external fields. Moreover, this method gives nonperturbative observation and analysis of single objects in a solution, which offers the possibility for easy trapping, real time analysis and visualization, easy integration with additional microenvironment control systems.[32]

Hydrodynamic trapping of suspended objects in fluids was first demonstrated by Taylor in 1934,[33] which was known as "four-roll mill" method. For decades, researchers have improved the original method to extend its ability for multiple types of fluid flows.[34–37] Recent efforts focused more on integrating computer based feedback control with the microfluidic chip, aiming to pro-

[a] Department of Mechanical Engineering, University of Washington, Seattle, WA 98195, USA.
[b] Micro/Bio/Nanofluidics Unit, Okinawa Institute of Science and Technology Graduate University, 1919-1 Tancha, Onna-son Okinawa, 904-0495 Japan. E-mail: amy.shen@oist.jp
[c] Department of Mechanical Engineering, The University of British Columbia, 2054-6250 Applied Science Lane, Vancouver, BC, V6T 1Z4, Canada.
[d] Chemical Engineering, Stanford University, Stanford, CA 94305-4125,USA.
† Electronic Supplementary Information (ESI) available: [details of any supplementary information available should be included here]. See DOI: 10.1039/b000000x/
‡ These authors contributed equally to this work.

vide controllability and fine tuning of micron objects under extensional flows.[38–40] Especially, controlled pneumatic technique by regulating force field is a well known method for the non-contact trapping of isolated targets. The pneumatic valve is referred to as the Quake's valve[41], which involves multilayered soft lithography (MSL). The liquid flows in the bottom layer (fluid layer) of the device, while the upper layer (control layer) pushes down the thin membrane polydimethhlsiloxane (PDMS) in the bottom layer by regulating the pressure inside the control layer. Based on this operating principle, components such as on-off valves, switching valves, metering valves, mixers and pumps can be designed in the microfluidic device for versatile flow control.[42] Furthermore, by carefully regulating the air pressure in the control layer, small objects (e.g. particles, cells, and long chain molecules) can be trapped hydrodynamically at the stagnation point created by an extensional flow.[43] Utilizing similar flow control techniques, cell/particle sorting[44] and further cell/particle manipulation[45,46] by the hydrodynamic force can be achieved.

1.2 Temperature control

Since temperature variations significantly affect the intrinsic properties of fluids, on-chip temperature control is necessary for stable operations inside microfluidic devices. Existing global temperature control methods either preheat the carrying fluid[47] inside the device, or use a printed wiring board (PWB) heating unit under the entire microfluidic device[48]. Localized temperature control methods have used either micropatterning wire on silicon[20,49,50] or micropatterning wire on glass[51–54] embedded in the device. While precise temperature control can be accomplished by using global temperature control for devices on the order of ~ 10 mm, it is challenging to achieve precise localized temperature control in a small and confined area ($\sim 10\ \mu\mathrm{m}^2$). Furthermore, the global temperature control usually measures the temperature outside the microchannel by using a thermocouple and utilizes a Peltier element to manipulate the temperature stage, leading to inaccurate temperature measurement inside the microchannel and causing slow cooling and heating at a rate around 10 °C/min, with temperature stability in the range of 1 °C.[55] As thermo-responsive physical phenomenon have drawn much attention in applications such as the stimuli of thermoresponsive polymers,[56] biological membrane response to temperature,[57] polymerase chain reaction (PCR),[18,19] and chemical reactions occuring at micron scales[18,20,21]. Microfabrication technology has enabled advances in accurate temperature control and manipulation inside microchannels with temperature ramp rates ranging from 0.1 to 20 °C per second and constant temperature gradients along the direction of the channel width from 6 to 40 °C/mm,[58] which allows more accurate investigations of thermal effects in microfluidic experiments.

1.3 Integrated control features

Although controlling individual microenvironment parameters has shown promising success, managing multiple microenvironment parameters with isolated targets (e.g., trapping target particles while manipulating the pH or temperature simultaneously),

is still challenging. Commercial temperature stages have been coupled with flow control devices to control millimeter sized heating zones, but not for localized micron size features.[55] Progresses in simultaneous localized flow and temperature control on a single chip can provide unique opportunities to improve our understanding of fundamental fluid mechanics and biomechanics problems, such as transient interfacial dynamics between partially miscible fluids, and measurement of instantaneous cell stiffness in-situ.

Taking steps forward to design an integrated microfluidic platform with both flow and temperature control features, we construct and report a specific microfluidic platform which consists of a flow-focusing channel for the generation of emulsion droplets and subsequent trapping in a cross junction, pressure control, and localized temperature control to demonstrate the working principle of our platform, with the goal of (1) trapping and manipulating of isolated targets by a precise pressure feedback control, (2) thermal management at the specific zone by a temperature feedback control, and (3) real time image processing and analysis for tracking the location and observing the morphological change of the isolated objects.

This paper is organized as follows. Section 2 provides fabrication procedures of the microfluidic device, schematics of the control system, information of the hardware used for on-chip feedback control. Section 3 introduces specific design criteria of the integrated platform involving both flow and localized temperature control. Section 4 showcases the device performance criteria *e.g.*, condition and stability of droplet generation and trapping, precision and accuracy of temperature control, and discusses factors affecting the control performances, followed by a validation experiment with aqueous glycerol and liquid crystal to demonstrate the working principle of the integrated microfluidic platform. Section 5 summarizes the features of our integrated microfluidic platform, with an outlook and potential applications.

2 Materials and methods

2.1 Device fabrication

We use standard multilayered soft-lithography (MSL)[41] protocols for fabrication of microfluidic channel and the wet etching process for conductive wire micropatterning. The device fabrication consists of several core steps below: conductive wire patterning on glass slides, double-layered PDMS microfluidic channel fabrication, and the device assembly (see schematic summary in **Fig. 1a**). More detailed fabrication procedure is discussed in ESI and the mask design is also available as a separate file in ESI.

2.2 Control systems

Simultaneous on-chip flow and temperature control is accomplished by employing a custom designed LabVIEW virtual interface that communicates with a gas regulator, temperature controller, and a digital multimeter (**Fig. 2**). The pressure regulation of pneumatic valves was achieved by using a gas regulator (Proportion-Air, QPV1), whose output has the maximum pressure of 150 psi with ±0.1% of setting output pressure accuracy. The output of the gas regulator was connected to the inlet port of the
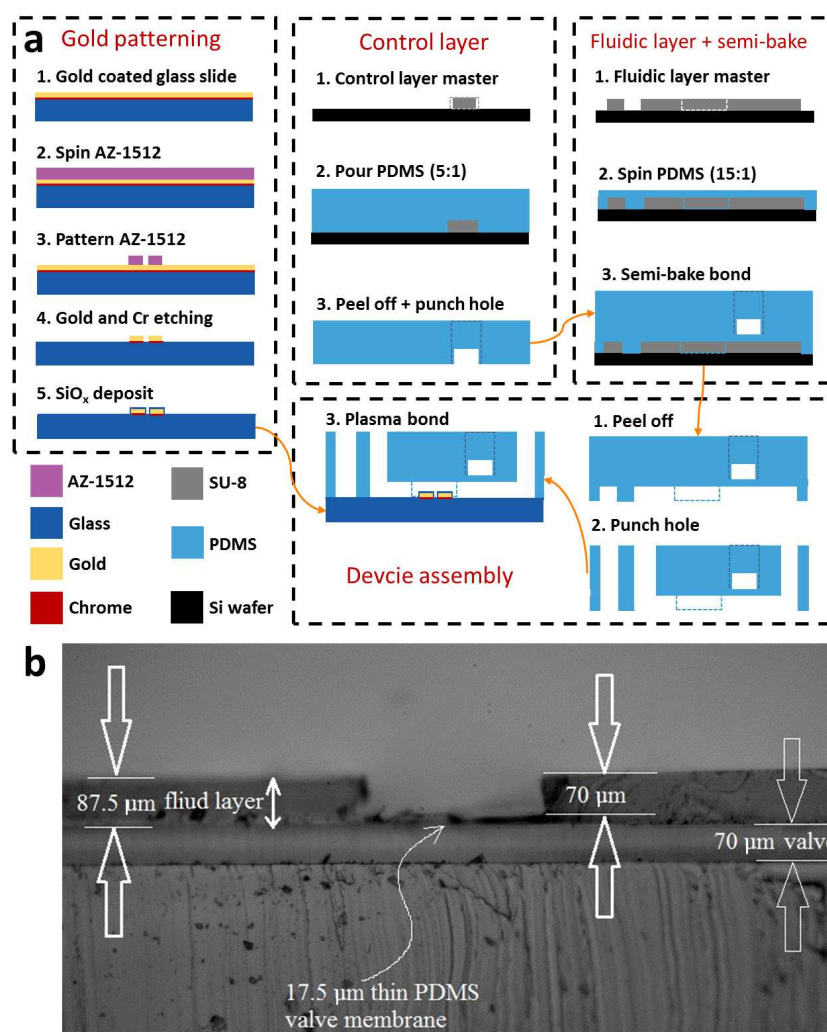
Fig. 1 Device fabrication and characterizations: (a) Cross-section view highlighting key device features, step-by-step procedure of conductive patterning, double-layered PDMS channel fabrication, and device assembly (see detailed descriptions in ESI); (b) Optical microscopy image of the cross section of the double-layered PDMS device, showing the structure of the membrane valve.

upper layer (control layer) in the device, when pressurized, deforming the elastomeric membrane in the the bottom layer (fluid layer) of the device, decreasing the cross section area of the fluidic channel. The pressure difference will be identical in every case. The gas regulator changes the flow resistance in one of the outlet channels, leading to a control of the flow rates in both channels, redistributing the planar extensional flow pattern, thus relocating the stagnation point position at the cross junction. Through active feedback control of the droplet position using the valve pressure, droplets can be trapped in the velocity potential well, created by actively manipulating the stagnation point of the extensional flow at the cross junction. A multifunction data acquisition module (National Instruments, PCI 6229) with a connection terminal (National Instruments, BNC 2110) is used as digital Input/Output (I/O) for the feedback control of the gas regulator. A high precision programmable power supply (BK Precision, 9124) is used as a power source for the microheater. A MOSFET switch module, controlled by the pulse width modulation (PWM) signal from a microcontroller board (Arduino, UNO-R3), was used for the fine

control over the heating power of the microheater. A digital multimeter (Keithley, 2700 with 1300 switch module) was used to measure the real time resistance of the temperature sensor, which can be converted to the temperature reading by the resistance-temperature relation obtained from the temperature sensor calibration. Syringe pumps (Cetoni, neMESYS Base 120) were used to pump fluids inside the microfluidic channel. The microfluidic chip was placed on an inverted microscope (Nikon, Eclipse Ti-U). Images were recorded by a high speed camera (Phantom vision research, M310) with the resolution of 256 by 320 pixels, 8-bit depth (256 gray levels), while having a real time image processing rate at 30 frames per second (fps) and up to 1,000 fps acquisition rate for transient phenomenon studies.

3 Design criteria of integrated platform

In this section, we show the rationale of design criteria of the integrated platform for both flow and localized temperature control. A specific integrated platform is developed to accomplish the following tasks on a single chip: generate size-specific emul-
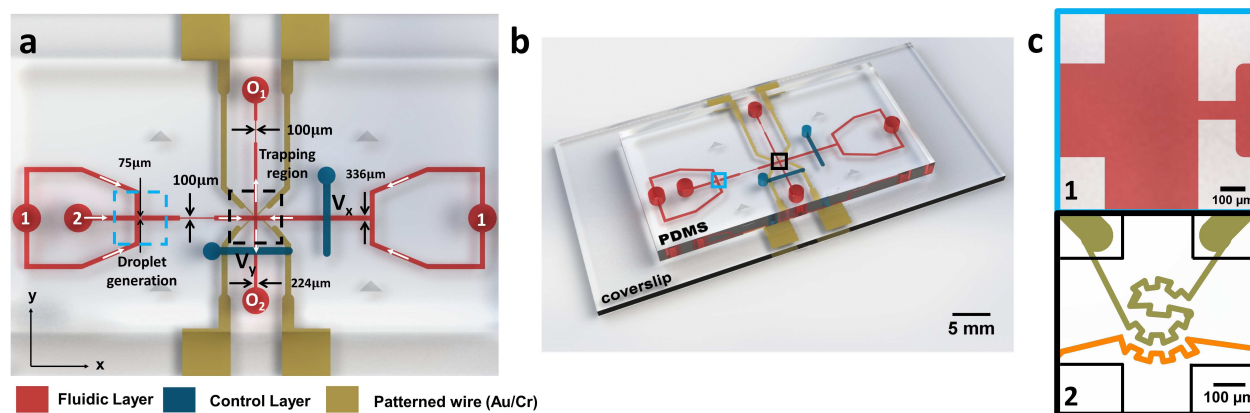
Fig. 3 Integrated microfluidic platform for both flow and localized temperature control: (a) plane view of the microfluidic device. The continuous and dispersed phases are introduced through inlet (1) inlet and (2), respectively. Emulsion droplets are generated at the flow-focusing region (cyan box), which are then delivered and selectively trapped at the cross-slot junction (black box). After converging at the cross-slot junction, the fluids exit through outlet O_1 and outlet O_2. (b) 3D rendering illustration of the microfluidic device, showing the glass slide etched with gold wires (microheater in the black box region), double-layered PDMS with microchannels in a fluidic layer (in red), and the control layer for pressure manipulation (in blue). (c) Enlarged view of the boxed regions showing: c-1 flow-focusing region, and c-2 microheater (gold) and temperature sensor (orange) at the cross-slot junction.
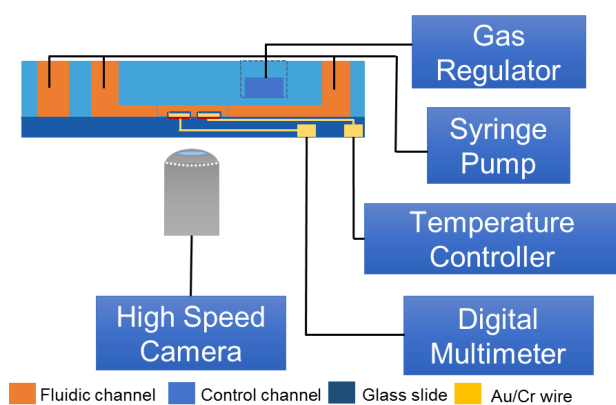

Fig. 2 Schematics of flow and temperature control systems in the microfluidic platform: A gas regulator controls the fluid resistance in the fluidic channel by regulating the pressure inside the control channel. A syringe pump introduces fluid flow inside the fluidic channel. A temperature controller and a digital multimeter are connected to the micropatterned wires (Gold/Chrome). The microfluidic platform is placed on an inverted microscope equipped by a high speed camera (Phantom Miro 310, vision research). The entire system is remotely controlled by a custom designed LabVIEW virtual interface.

sion droplets with the flow focusing geometry, hydrodynamically deliver and trap one droplet at the stagnation zone of the cross-junction by modulating the cross section area of the microchannel with active feedback control. Once the droplet trapping is achieved, the temperature is locally mediated on chip with a localized microheater, controlled by a temperature controller. Upon initiating data acquisition, the morphological change of the droplet and the temperature profile can be recorded in real time at the specific region of interest. The schematics of this microfluidic platform is illustrated in **Fig. 3**. The microfluidic channel (**Fig. 3**) consists of two core regions: flow focusing region (**Fig. 3c-1**) for emulsion droplet generation, and the cross-slot

junction (**Fig. 3c-2**) in the center of the platform for droplet trapping. Furthermore, a conductive circular patterned wire (**Fig. 3c-2**), acting as a localized microheater and temperature sensor, is placed in the center of the cross junction region for precise temperature control of the trapped droplet.

3.1 Integrated flow control

The integrated platform has two patterned PDMS layers, a thin fluidic layer forming passage way for fluid flow and a thick layer containing two pneumatic valves. The fluidic layer (**Fig. 3a**, highlighted in red) has three inlets, two for the continuous phase and one for the dispersed phase, with a flow focusing junction (**Fig. 3a**, box in cyan) for droplets generation, and a cross-slot junction (**Fig. 3a**, box in black) for subsequent droplet trapping. The inlet streams flow, from each half, in opposing direction towards the cross-slot junction, converge, then exit via two outlets (O_1 and O_2 in **Fig. 3a**). The control layer has two dead-end channels sitting perpendicular to the fluidic channel, forming the pneumatic channels with elastomeric membrane valves. By regulating the pressure inside a pneumatic channel of the control layer, the cross section area of fluidic channel underneath can be modulated, leading to changes in the fluidic resistance at the valve section.

3.1.1 Emulsion droplet generation

The formation of uniform sized emulsion droplets is enabled by using a flow-focusing design. The microfluidic channel consists of two inlets, labeled as (1) for the continuous phase and (2) for the dispersed phase (**Fig. 3a**). The continuous and dispersed phases flow from both sides to the cross-junction. By controlling the flow rate ratio between the two phases, dispersed phase droplets with uniform sizes are continuously generated. The orifice of the flow-focusing channel is 75 μm and 100 μm in width and height, respectively.

3.1.2 Droplet trapping

Once the emulsion droplets are produced, they flow towards the cross junction area and the flow bifurcates from the cross-junction to the two outlets. The width and height of the cross-junction are 350 μm and 232 μm. Gas regulators control the fluid resistance in the fluidic channel by regulating the pressure inside the control channel. A syringe pump introduces fluid flow inside the fluidic channel. Two pneumatic valves with 500 μm in width are located at the horizontal and perpendicular direction of the microchannel labeled as V_x and V_y. These valves can be controlled by gas regulators that control the pressure in the control channels to block the cross-section of the microchannels. This modulates the fluid resistance inside the fluidic channels, manipulating the position of the stagnation point along the x- and y-directions.

3.1.3 Flow control

The control program for the hydrodynamic trapping of particles was first developed by Tanyeri et. al. [43] by using LabVIEW. We built upon their program with our customized hardware setup. We also optimized the algorithm for real-time image processing of trapped droplets at the cross-junction to remove the optical background introduced by the microheater and the temperature sensor embedded in the device.

A region of interest (ROI) was defined at the center of the cross-junction to establish a set point and spatial limits for real-time image processing within the field of view. The center of the ROI (x_t, y_t) corresponds to the user-defined trapping position of the droplet. The real-time images could be adjusted by controlling the threshold of the image to enhance the image contrast and identify the edge of the droplet. The pre-processed images were then converted into binary images after implementing a series of morphology processing with a built-in particle analysis function in LabVIEW (more details about real time image processing is available in SI). The center of the droplet (x_c, y_c) obtained by the image analysis was considered as the current position of the droplet. The trapping error was defined as $e_x = x_c - x_t$ and $e_y = y_c - y_t$ along the x- and y-direction. Once the droplet was trapped in the ROI, the controller automatically compensated the trapping error with a customized proportional control algorithm.

3.2 Localized temperature control

The microheater (**Fig. 3c-2**, highlighted in gold) is designed in a zigzag pattern with a circular heating zone for efficient heating, with the dimension $\sim$ 20 μm, 900 μm, and 200 μm in width, length, and diameter, respectively. The temperature sensor is etched adjacent to the microheater on chip (**Fig. 3c-2**, highlighted in orange), with feature dimensions approximately $\sim$ 20 μm, 430 μm, and 20 μm in width, length, and gap from the microheater, respectively. The circular geometry of the microheater is important, as it allows the access for droplet edge detection in real time image processing. These heater and sensor geometries also enable good heating uniformity and precise localized temperature sensing in application scenarios with circular object. [59]

The sensing of the temperature change is achieved by measuring the change of resistance in the sensor as the microheater heats

up the fluid and glass substrate first, with the temperature change of the fluid and glass substrate altering the resistance on the temperature sensor. Thus, monitoring and manipulating the temperature in a local region as small as hundreds of μm is possible with our active feedback control procedure. We developed the virtual instrument operation interface by LabVIEW for the monitoring and manipulation of localized temperature, achieving an active feedback control between the microheater and the temperature sensor. A temperature setpoint was defined by user as the set temperature (T_s). The current temperature (T_c) was obtained by transferring sensor resistance to real time temperature reading, using the temperature calibration curve (see subsection below). The temperature error was defined as $e_T = T_c - T_s$, which is compensated to converge to zero via a built-in proportional-integral-derivative (PID) control algorithm.

4 Results and discussions

4.1 Droplet trapping performance

Even though trapping solid particles such as polystyrene beads and cells are already reported, it is more challenging to trap emulsion droplets due to the following reasons. First, the size of the droplet produced at the flow-focusing device (on the order of tens to hundreds of microns) is comparatively larger than that of a polystyrene bead for trapping purposes. In addition, the density of certain liquids (i.e., liquid crystal) can be 30 % higher than that of polystyrene, thus the larger mass and hence inertia from the droplet can lead to difficulty when trapping the droplet using the pressure difference with the pneumatic valve. Second, the droplet trapping involves liquid/liquid interfaces between the two liquid phases, which introduces additional instability to the system. Due to these difficulties, the following issues should be resolved to achieve successful droplet trapping: (1) establishing the optimal droplet generation conditions at the flow-focusing region, and (2) stablizing the trapped droplet with respect to flowing liquids. In the following two subsections, we demonstrate the influence of droplet generation conditions and flow rate conditions on the droplet trapping performance.

4.1.1 Influence from droplet generation

To explore the influence of droplet generation conditions on the trapping performance, we used oleic acid with a small amount of Span 80 (0.1 wt%) as the continuous phase, and 50 wt% aqueous glycerol solution as the dispersed phase in the microfluidic channel. Flow rates are varied from 8 $\mu l/hr$ to 1000 $\mu l/hr$ to produce the aqueous droplet with varying sizes. The droplet generation occurs either in the dripping regime or the jetting regime. [60,61] The dripping regime occurs at relatively low flow rates and is characterized by the periodic formation of highly uniform spherical droplets. Due to the competition between the viscous and capillary forces, the dispersed phase breaks into discrete droplets periodically under certain flow rate ratios. The droplet production is mainly governed by the flow rate ratio, viscosity ratio, and the capillary number ($Ca = \eta_0 V_0 / \sigma_i$), where η_0 is the dynamic zero shear viscosity of the continuous phase, V_0 is the average velocity of the continuous phase at the orifice, and σ_i is the interfacial tension between the dispersed and continuous phases. Gen-

erally, droplet diameters are proportional to the ratio between the interfacial tension and the viscous force exerted from the continuous phase.[62,63] With increasing flow rates of both phases, the dripping regime gives way to a jetting regime, which features a long jet that stretches downstream (**Fig. 4b4**). Jetting is a con-
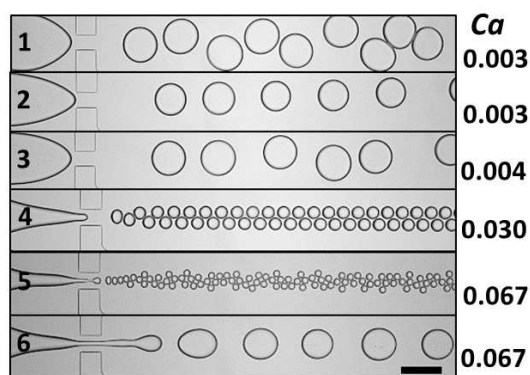

Fig. 4 Droplet production with varying flow rates: Oleic acid droplet produced at aqueous glycerol solution with varying flow rates ratio (dispensed phase/continuous phase) (1) 0.16, (2) 0.8, (3) 0.667, (4) 0.11, (5) 0.1 (6) 0.2. Scale bars are 200 μm

sequence of the increased flow rates that force the filament to travel at a greater rate. Unlike in the dripping regime, droplets do not form at the orifice, but instead form at the tip of the jet farther downstream. In general, the length of the jet will increase with increasing flow rates of both phases. Meanwhile, the jet becomes quite thick and produces larger droplets than in the dripping regime. We show that it is possible to generate droplets as small as 10 μm – 30 μm in diameter. However, the distance between these traveling droplets becomes much shorter, which causes obstacles in trapping droplets at the cross-junction due to drop–drop interaction.

4.1.2 Flow rate effects

The hydrodynamic trapping relies on the extensional flow at the cross-junction to balance against the Brownian motion and flow fluctuations, by applying appropriate pressure using pneumatic valves to confine the objects close to the stagnation point (zero-velocity and zero-velocity-potential point). Planar extensional flow is generated in the cross-junction channel by introducing two laminar streams, which can create a stagnation point at the center of the cross-junction region. The stagnation point is a semi-stable point (stable along x direction but unstable along y direction), whose velocity potential (φ)[32] and fluid velocity vector (**u**)[43] can be expressed as

$$\varphi = \left(\frac{\dot{\varepsilon}}{2}\right)\left(x^2 - y^2\right), \tag{1}$$

$$\mathbf{u} = -\left(\frac{\partial \varphi}{\partial x}, \frac{\partial \varphi}{\partial y}\right) = (-\dot{\varepsilon}x, \dot{\varepsilon}y), \tag{2}$$

where $\dot{\varepsilon}$ is the strain rate (s^{-1}), x and y are the spatial coordinates with respect to the stagnation point along the inlet and outlet. Equation (1) entails that the stagnation point is a semi-stable point (saddle point). Equation (2) reveals the relationship

between the velocity vector field **u** and the potential field φ. In principle, with an active feedback control, it's possible to transfer a localized maximum zero-velocity-potential point into localized minimum zero-velocity-potential point along y direction. As a result, the stagnation point can be rendered from a saddle point to a stable critical point, conserving a potential well for steady hydrodynamic trapping[32].

To trap larger objects at the cross-junction, one can either increase the proportional control gain (K_p) from the LabVIEW code or increase the flow rate of the fluid. However, both strategies have their limitations. The control signal output for pneumatic valve regulation is proportional to the proportional control gain (K_p), correlated with the trapping error. For larger K_p, the controller is prompted to eliminate the error by adjusting the fluid resistence of the outflowing stream, as a result, moving the stagnation point corresponding to modified extensional flow at the cross junction. Large K_p may lead to sufficient disturbances in the extensional flow to prevent droplet trapping. Increasing the flow rate of the fluid provides larger driving force by generating sharper velocity potential distributions, which requires higher image resolution and short feedback cycle to achieve steady trapping. The working principle to strike a fine balance between K_p and flow rates is illustrated in **Fig. 5 A**. **Fig. 5 A (a–h)** shows a series of histograms of the trapping error along the Y direction with flow rates ranging from 65–290 μ l/hr. With perfect trapping, the error distribution should form a sharp peak around Y=0. When the trapping becomes unstable, the trapping errors exhibit a wide distribution with a flat peak. **Fig. 5 A** shows that the droplet trapping becomes unstable when the flow rate exceeds 240 μ l/hr. Moreover, the deformation of the droplet becomes more significant as the flow rate increases, see **Fig. 5 B**. These results demonstrate that the steady hydrodynamic trapping for droplets is possible by creating a potential well using the extensional flow and regulation of the pressure by the pneumatic valve.

4.2 Localized temperature control performance

To evaluate the localized temperature control performance, we ran an aqueous glycerol solution (65 wt%) through the device and set the temperature to 35 °C. After the temperature was stabilized, we maintained the temperature at 35 °C for 2 min, while acquiring localized temperature sensing data. Figure 7 shows the results. The temperature varied as little as ±0.25°C with a low relative standard deviation ($\sigma = 0.083$ °C).

4.3 Design validation experiment

To demonstrate the capabilities of our integrated microfluidic platform with both flow and temperature control, we selected a thermotropic liquid crystal (LC), 4-Cyano-4'-pentylbiphenyl (5CB) as the droplet phase for the proof of concept studies since 5CB undergoes rapid and reversible nematic-to-isotropic transition at approximately 35°C.[64] An aqueous glycerol solution (65 wt%) with 3.5 mM of the surfactant Sodium dodecyl sulfate (SDS) was used as the continuous phase. The flow rates of the continuous and dispersed phases were initially adjusted to be 200 μL/hr and 10 μL/hr to generate uniform sized LC droplets
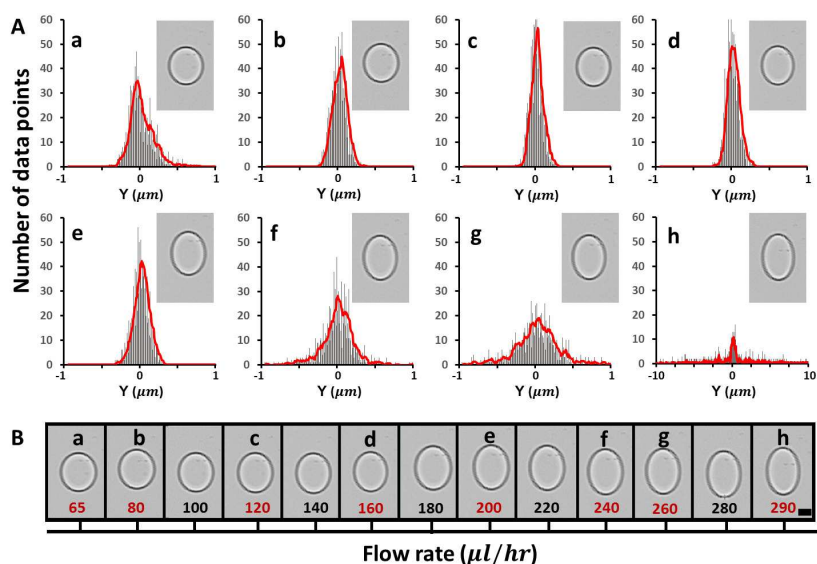
Fig. 5 Influence of the flow rate to droplet trapping and morphology: (A) The histogram of droplet trapping error along the Y direction at selected continuous phase flow rates; (B) Microscopy images exhibiting droplet deformation under different flow rates. Scale bar is 50 μm.
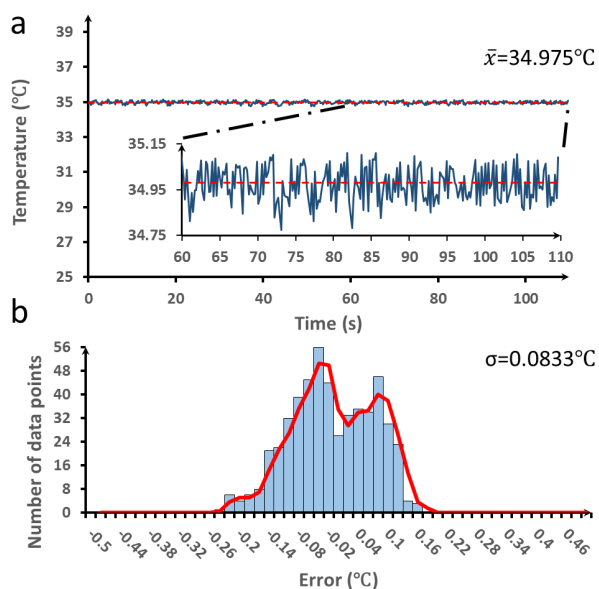

Fig. 6 Temperature control performance: (a) The temperature variation evaluation of the temperature control, when setting the target temperature at $35°$C for 2 min. The variation is within $\pm0.25°$C. $\bar{x}$ is the mean value of the temperature obtained; (b) Histogram of localized temperature control error. The error is defined as $T_c - T_s$. σ stands for the relative standard deviation of the error.

Fig. 7 Liquid crystal droplet generation and trapping: (a) image sequences showing liquid crystal droplet generation under polarized light. Scale bar is 100 μm; (b) liquid crystal droplet trapped at the cross junction. Scale bar is 100 μm; (c) Microscopy images showing morphology of liquid crystal droplet under polarized light at rest (left), under unpolarized light at rest (middle), and under polarized light of a moving droplet (right).

with a diameter around 110 μm at the flow-focusing junction, at room temperature (**Fig. 7a**).

Once nematic LC droplets were generated at the flow-focusing region, they continued to flow towards the cross junction zone, with the flow rate of the LC phase being reduced to zero to avoid possible coalescence between the trapped LC droplet and flowing LC droplets. The on-chip pneumatic valve was used to regulate the relative flow resistance in the outlet streams, which enables
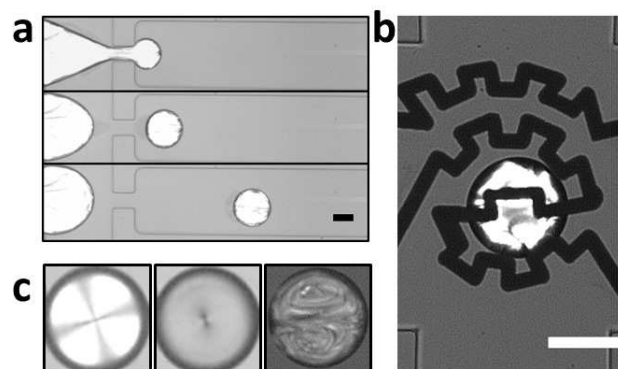
fine control of the position of the stagnation point for easier trapping. At the cross-junction of the microchannel, the nematic LC droplet with diameter of 110 μm was successfully recognized and trapped (**Fig. 8a**), by employing real time image processing using built-in edge detection and particle analysis algorithm (see SI video). A region of interest (ROI) within the imaging window was defined to establish a set point and spatial limits for real-time image processing within the field of view. In this experiment, an initial pressure of the pneumatic valve was set to 1 psi which was regulated via the LabVIEW GUI. The trapped nematic LC droplet was confined in the ROI within the tolerance of $\pm3\mu$m using a proportional controller (Kp=-0.01).

Upon trapping, the temperature of the microheater underneath the trapped LC droplet was increased from room temperature to 35 °C, with the aid of the temperature controller. A polarized
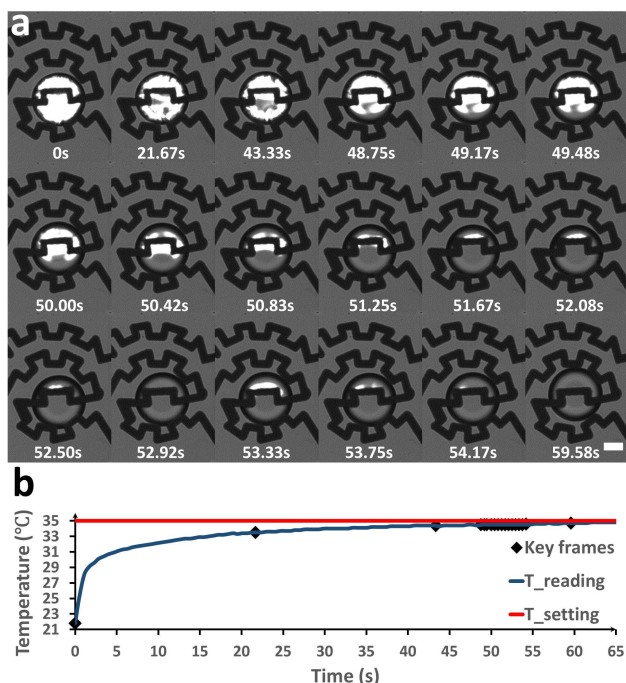
Fig. 8 Nematic-to-isotropic transition of LC droplet with localized temperature control: (a) the LC droplet shows nematic-to-isotropic transition with increasing temperature (correlated with elapsed time), with the scale bar= 50 μm. (b) The temperature profile obtained by the temperature sensor, corresponding to captured key frames.

feedback control with multiple hardware Inputs/Outputs (I/O). The LC droplet exhibited its nematic-to-isotropic transition with increasing temperature. The temperature variation was found to be as small as ± 0.25°C with a relatively low standard deviation, which guarantees precise control of the temperature within a local region.

Our integrated microfluidic platform offers great potentials to provide direct real-time flow and temperature control that is critical to characterize transient interfacial dynamics in miscible jets and pendant drops, and in the dissolution of sessile drops, relevant to numerous technological processes, ranging from cleansing operations where liquid soaps are rinsed from surfaces, to the dissolution of mucous in the intestinal tract.

Another potential area of applications involves biotechnology, such as on-chip cellular physiology studies with droplet based on-chip rapid PCR applications. Although high throughput on-chip cell culture and monitoring have been reported in literature,[15–17] isolating and monitoring single cells while manipulating multiple variables in a localized microenvironment is still challenging. For example, with current digital PCR technology, despite its ability to process thousands single cell laden droplets simultaneously, it does not permit dynamic monitoring of single cell responses with complex reaction steps[65]. Our microfluidic platform, with instantaneous flow and localized temperature control features, provides great potentials to manipulate the location and microenvironment of selected single cells precisely, which is essential for dynamic monitoring of single cell responses under more complex reaction procedures at longer time periods.[66,67] Our proof-of-concept studies with LC droplets demonstrated the capability to trap isolated micron size target while manipulating localized temperature environment precisely with high sensitivity and quick response (15 °C/min with both ramp-up and cool-down cycles, with temperature overshoot less than 2 %). We also demonstrated the temperature control ability in our platform at relatively high temperatures in a wide temperature range to simulate a single PCR cycle, proving the accessibility of high temperature (up to 95°C) control with our platform (see details in ESI). With proper modifications, we envision a similar microfluidic platform can be designed to study isolated single cells[68].

optical microscope was used to capture the nematic-to-isotropic transition of the LC droplet with localized temperature variations (**Fig. 8**). The LC droplet exhibited the nematic state initially at room temperature, and started the transition into the isotropic state at 21.67 sec as the temperature reached around 33 °C. The LC droplet became transparent at 59.58 sec as the temperature reached 35 °C, indicating the complete nematic-to-isotropic transition of the LC droplet. This process is reversible and our experiments show reproducibility (see Movie S2: LC morphology transition under periodic temperature profile in SI video).

5 Conclusions and perspective

We developed an integrated microfulidic platform which consists of a flow-focusing channel for the generation of emulsion droplets, with instantaneous flow and localized temperature control. A double-layered microfluidic channel was fabricated, and integrated with the microheater and temperature sensor to control the flow and temperature simultaneously. Both flow and temperature were manipulated by the LabVIEW with active feedback control. In particular, we used thermotropic liquid crystal (LC) as the droplet phase to demonstrate the temperature control capacity of our integrated microfluidic platform as a proof-of-concept experiment. The liquid crystal droplet was successfully trapped at the cross-junction of the channel with a pneumatic valve regulated by LabVIEW feedback control with the proportional air pump. The temperature was mediated by the microheater and the temperature sensor underneath the LC droplet by the LabVIEW

Acknowledgement

References

1 G. Whitesides, *Nature*, 2006, **442**, 368–373.

2 H. Bruus, *Theoretical microfluidics*, Oxford : Oxford University Press, Oxford, 2008.

3 G. Karniadakis, *Microflows and nanoflows : fundamentals and simulation*, New York, NY : Springer, New York, NY, 2005.

4 D. J. Beebe, G. A. Mensing and G. M. Walker, *Annual Review of Biomedical Engineering*, 2002, **4**, 261–286.

5 G. Velve-Casquillas, M. Le Berre, M. Piel and P. T. Tran, *Nano Today*, 2010, **5**, 28–47.

6 J. Leng and J.-b. Salmon, *Lab on a Chip*, 2009, **9**, 24–34.

7 Y. Tanaka, K. Sato, T. Shimizu, M. Yamato, T. Okano and T. Kitamori, *Biosensors and bioelectronics*, 2007, **23**, 449.

8 S. Okushima, T. Nisisako, T. Torii and T. Higuchi, *Langmuir*, 2004, **20**, 9905–9908.

9 Z. Nie, W. Li, M. Seo, S. Xu and E. Kumacheva, *Journal of the American Chemical Society*, 2006, **128**, 9408–9412.

10 H. Song, J. D. Tice and R. F. Ismagilov, *Angewandte Chemie*, 2003, **115**, 792–796.

11 S. Koster, F. E. Angile, H. Duan, J. J. Agresti, A. Wintner, C. Schmitz, A. C. Rowat, C. A. Merten, D. Pisignano, A. D. Griffiths and D. A. Weitz, *Lab Chip*, 2008, **8**, 1110–1115.

12 L. R. Huang, E. C. Cox, R. H. Austin and J. C. Sturm, *Science*, 2004, **304**, 987–990.

13 D. R. Gossett, H. T. K. Tse, S. A. Lee, Y. Ying, A. G. Lindgren, O. O. Yang, J. Rao, A. T. Clark and D. Di Carlo, *Proceedings of the National Academy of Sciences*, 2012, **109**, 7630–7635.

14 T. T. Perkins, D. E. Smith and S. Chu, *Science (New York, N.Y.)*, 1997, **276**, 2016.

15 I. Meyvantsson and D. J. Beebe, *Annual Review of Analytical Chemistry*, 2008, **1**, 423–449.

16 N. Li, A. Tourovskaia and A. Folch, *Critical Reviews in Biomedical Engineering*, 2003, **31**, 423–488.

17 S. Takayama, J. McDonald, E. Ostuni, M. Liang, P. Kenis, R. Ismagilov and G. Whitesides, *Proceedings Of The National Academy Of Sciences Of The United States Of Ame*, 1999, **96**, 5545–5548.

18 A. Jain and K. E. Goodson, *Journal of Thermal Biology*, 2011, **36**, 209–218.

19 G. Maltezos, A. Gomez, J. Zhong, F. A. Gomez and A. Scherer, *Applied Physics Letters*, 2008, **93**, 243901.

20 A. I. K. Lao, T. M. H. Lee, I. M. Hsing and N. Y. Ip, *Sensors and Actuators a-Physical*, 2000, **84**, 11–17.

21 A. Manz, N. Graber and H. M. Widmer, *Sensors and Actuators B-Chemical*, 1990, **1**, 244–248.

22 D. Di Carlo, D. Irimia, R. G. Tompkins and M. Toner, *Proceedings of the National Academy of Sciences*, 2007, **104**, 18892–18897.

23 M. Yamada, M. Nakashima and M. Seki, *Analytical chemistry*, 2004, **76**, 5465–5471.

24 L. R. Huang, E. C. Cox, R. H. Austin and J. C. Sturm, *Science*, 2004, **304**, 987–990.

25 E. Chmela, R. Tijssen, M. T. Blom, H. J. Gardeniers and A. van den Berg, *Analytical chemistry*, 2002, **74**, 3470–3475.

26 M. Evander, L. Johansson, T. Lilliehorn, J. Piskur, M. Lindvall, S. Johansson, M. Almqvist, T. Laurell and J. Nilsson, *Anal. Chem.*, 2007, **79**, 2984–2991.

27 H. M. Hertz, *Journal of Applied Physics*, 1995, **78**, 4845–4849.

28 A. Yang, S. D. Moore, B. S. Schmidt, M. Klug, M. Lipson and D. Erickson, *Nature*, 2009, **457**, 71–75.

29 A. E. Cohen, *Physical Review Letters*, 2005, **94**, 118102.

30 B. G. Hosu, K. Jakab, P. Banki, F. I. Toth and G. Forgacs, *Review of Scientific Instruments*, 2003, **74**, 4158–4163.

31 V. H. Lieu, T. A. House and D. T. Schwartz, *Analytical Chemistry*, 2012, **84**, 1963–1968.

32 M. Tanyeri and C. M. Schroeder, *Nano Letters*, 2013, **13**, 2357–2364.

33 G. I. Taylor, *Proceedings of the Royal Society of London. Series A, Containing Papers of a Mathematical and Physical Character (1905-1934)*, 1934, **146**, 501–523.

34 L. Joo Sung, D.-S. Rebecca, P. T. Nerayo and J. M. Susan, *Applied Physics Letters*, 2007, **90**, 074103.

35 P. Start, S. D. Hudson, E. Hobble and K. Migler, *J. Colloid Interface Sci.*, 2006, **297**, 631–636.

36 S. D. Hudson, F. Phelan, M. D. Handler, J. Cabral, K. Migler and E. Amis, *Appl. Phys. Lett.*, 2004, **85**, 335–337.

37 B. J. Bentley and L. G. Leal, *J. Fluid. Mech.*, 1986, **167**, 219–240.

38 C. Schroeder, R. Teixeira, E. Shaqfeh and S. Chu, *Physical Review Letters*, 2005, **95**, 025025.

39 C. M. Schroeder, H. P. Babcock, E. S. G. Shaqfeh and S. Chu, *Science (New York, N.Y.)*, 2003, **301**, 1515.

40 D. Smith, H. Babcock and S. Chu, *Science*, 1999, **283**, 1724–1727.

41 M. A. Unger, H. P. Chou, T. Thorsen, A. Scherer and S. R. Quake, *Science (New York, N.Y.)*, 2000, **288**, 113.

42 K. A. Anthony, L. Hoyin, R. U. Ben and F. Albert, *Micromachines*, 2011, **2**, 179.

43 M. Tanyeri, M. Ranka, N. Sittipolkul and C. M. Schroeder, *Lab on a Chip*, 2011, **11**, 1786–1794.

44 C. Wyatt Shields Iv, C. D. Reyes and G. P. Lpez, *Lab Chip*, 2015, **15**, 1230–1249.

45 T. Yasukawa, K. Nagamine, Y. Horiguchi, H. Shiku, M. Koide, T. Itayama, F. Shiraishi and T. Matsue, *Analytical Chemistry*, 2008, **80**, 3722.

46 I. Barbulovic-Nad, H. Yang, P. S. Park and A. Wheeler, *Lab Chip*, 2008, **8**, 519–526.

47 G. Velve Casquillas, C. Fu, M. Le Berre, J. Cramer, S. Meance, A. Plecis, D. Baigl, J. J. Greffet, Y. Chen, M. Piel and P. T. Tran, *Lab Chip*, 2011, **11**, 484–9.

48 K. Lian, S. O'Rourke, D. Sadler, M. Eliacin, C. Gamboa, R. Terbrueggen and M. Chason, *Sensors and Actuators: B. Chemical*, 2009, **138**, 21–27.

49 D. Resnik, D. Vrtacnik, M. Mozek, B. Pecar and S. Amon, *Journal of Micromechanics and Microengineering*, 2011, **21**, 018301.

50 H. Yang, C. A. Choi, K. H. Chung, C. H. Jun and Y. T. Kim, *Analytical Chemistry*, 2004, **76**, 1537–1543.

51 K. S. Lee, P. Boccazzi, A. J. Sinskey and R. J. Ram, *Lab Chip*, 2011, **11**, 1730–9.

52 V. Bazargan and B. Stoeber, *J. Microelectromech. Syst.*, 2010, **19**, 1079–1087.

53 H. Bridle, M. Millingen and A. Jesorka, *Lab Chip*, 2008, **8**, 480–3.

54 L. Y. Liu, S. L. Peng, W. J. Wen and P. Sheng, *Applied Physics Letters*, 2007, **91**, 093513.

RSC Advances Accepted Manuscript

55 J. D. Adams, C. L. Ebbesen, R. Barnkob, A. H. J. Yang, H. T. Soh and H. Bruus, *Journal of Micromechanics and Microengineering*, 2012, **22**, 075017.

56 H.-i. Lee, J. Pietrasik, S. S. Sheiko and K. Matyjaszewski, *Progress in Polymer Science*, 2010, **35**, 24–44.

57 L. Atia and S. Givli, *Journal of The Royal Society Interface*, 2014, **11**, 20131207.

58 V. Miralles, A. Huerre, F. Malloggi and M.-C. Jullien, *Diagnostics*, 2013, **3**, 33–67.

59 P. Bhattacharyya, *IEEE Trans. Device Mater. Reliab.*, 2014, **14**, 589–599.

60 L. Rayleigh, *Proceedings of the Royal Society of London (1854-1905)*, 1879, **29**, 71–97.

61 P.-G. d. Gennes, *Capillarity and wetting phenomena : drops, bubbles, pearls, waves*, New York : Springer, New York, 2004.

62 L. A. Shelley, B. Nathalie and A. S. Howard, *Applied Physics Letters*, 2003, **82**, 364.

63 T. M. Squires and S. R. Quake, *Reviews of Modern Physics*, 2005, **77**, 977–1026.

64 B. Hamlington, B. Steinhaus, J. Feng, D. Link, M. Shelley and A. Shen, *Liquid Crystals*, 2007, **34**, 861–870.

65 H. Yin and D. Marshall, *Current Opinion in Biotechnology*, 2012, **23**, 110–119.

66 J. Nilsson, M. Evander, B. HammarstrÃűm and T. Laurell, *Analytica Chimica Acta*, 2009, **649**, 141–157.

67 A. Theberge, F. Courtois, Y. Schaerli, M. Fischlechner, C. Abell, F. Hollfelder and W. â. Huck, *Angew. Chem. Int. Ed.*, 2010, **49**, 5846–5868.

68 E. M. Johnson-Chavarria, U. Agrawal, M. Tanyeri, T. E. Kuhlman and C. M. Schroeder, *Lab on a Chip*, 2014, **14**, 2688–2697.